

Detection of the Permanent Strain Offset Component of Gravitational-Wave Memory in Black Hole Mergers

JEFFREY D. SCARGLE¹

¹*Astrobiology and Space Science Division
Planetary Systems Branch
NASA Ames Research Center
Moffett Field, CA 94035, USA
Jeffrey.D.Scargle@nasa.gov
jeffscargle@gmail.com*

ABSTRACT

This paper reports direct measurements of the permanent space-time strain offset component of the gravitational-wave memory predicted by general relativity to accompany black hole mergers. Such a change in strain, persisting after the wave itself is long past – measurable in principle but with considerable difficulty – has heretofore eluded detection. Since it is independent of the form of the time-development of the memory strain, this approach circumvents the need for precise modeling of the memory and non-memory signals. A model-independent analysis using a template-like algorithm, applied to a selection of 67 observations of 41 black hole merger events in the LIGO/Virgo Gravitational Wave Transient Catalog, yields a mixture of probable detections and upper limits. The associated statistical significance is assessed using parallel analysis of a large number of intervals shifted in time away from the mergers. The resulting p-value for a reasonably formulated null hypothesis (no real signals anywhere in the ensemble) is less than .003. Appendices contain MatLab code for the operations in the analysis, including an algorithm for the complex Fourier transform for arbitrarily spaced data.

Keywords: Gravitational Waves, Gravitational Memory, General Relativity

Contents

1. Gravitational-Wave Memory	3
1.1. Theory	3
1.2. Detection Issues	3
1.3. Measuring the Permanent Strain Offset	6
2. Data Selection and Pre-Processing	6
2.1. Data Selection	6
2.2. Centering the Merger Events	7
2.3. Whitening	7
2.4. Bandpass Filtering	8
2.5. Optimal Cleaning	8
2.6. Strain Calibration	8
3. Measuring the Strain Offset	9
3.1. Pre-Event and Post-Event Averaging Intervals	9
3.2. Averaging Methods	9
3.3. Results	10
3.4. Statistical Significance	13
4. Discussion	13
4.1. Hanford-Livingston Comparison	13

4.2. Preponderance of Reversion over Divergence	16
4.3. Previous Studies of Memory Observables	16
4.4. Conclusions	17
5. Appendix A: Strain Offset Measurements	22
6. Appendix B: Fourier Transform of Arbitrarily Spaced Data (Matlab Code)	24
7. Appendix C: Shift Merger Event to the Center of the Data Array	25
8. Appendix D: Shift Endpoints to Oscillation Nodes	26
9. Appendix E: Whitening with Tapers	28
10. Appendix F: Block Averaging of Amplitude Spectra a la Welch	30

1. GRAVITATIONAL-WAVE MEMORY

A gravitational wave induces spatial distortion, called *strain*, consisting of alternate compressions and expansions transverse to the wave. Consider the massive mirrors suspended in a laser interferometer – a practical realization of an ideal cluster of free-floating infinitesimal *test masses*. This detector senses changes in separations between the masses imposed by the gravitational wave. The prediction that such separations do not return to their initial values after the wave has passed is called *gravitational wave memory*. In black hole mergers the gravitational radiation itself is the source of memory via the *Christodoulou effect* (Christodoulou 1991; Thorne 1992).

While not necessarily small compared to the better known oscillatory “chirp” signal, detection of this effect has been heretofore elusive. One difficulty is that the instrumental and data analysis techniques necessary to suppress noise, also suppress some of the memory signal (cf. §1.2). It will be seen that this theoretically permanent signal is rendered effectively transient on roughly the same time scale as that of the chirp signal itself. Nevertheless the magnitude of the *permanent strain offset* can be directly measured, as reported here. Such a partial characterization of the memory effect, via measurement of only the final strain offset, or saturated value, should be useful for the detailed modeling and data analysis that will be necessary in the future to fully implement new tests of non-linear general relativity.

1.1. Theory

Early work (Braginsky and Thorne 1987; Thorne 1992) has spawned a growing body of research on linear and nonlinear (often called *ordinary* and *null*) memory (Favata 2010; Pollney and Reisswig 2011; Flanagan et al 2019, 2020; Bian, Cai, Cao et al. 2020; Grant and Nichols 2020; Liu, He and Cao 2021; Khera, Krishnan, Ashtekar and De Lorenzo 2021; Mitman, Iozzo, Khera et al. 2021; Zhang et al 2017; Divakarla and Whiting 2021; Kumar 2021). Two recent papers are of interest, while not directly relevant to this paper. Zhao and Cao (2021) discuss a potentially observable memory signature from mergers producing chirp signals at frequencies too low to be observed individually but accumulating stochastically to form a detectable background. Tiwari, Ebersold and Hamilton (2021) have discussed the role of tidal effects during mergers in producing memory signals that can help distinguish neutron star-black hole mergers from black hole-black hole mergers.

1.2. Detection Issues

The data usage notes at the Gravitational Wave Open Science Center (2020) include these warnings:

“Advanced LIGO and Virgo strain data are not calibrated below 10 Hz. ... Advanced LIGO detector noise rises rapidly below 10 Hz; it is many orders of magnitude larger than any plausible gravitational wave strain signal. Further, the data made available on GWOSC are aggressively high-pass-filtered at 8 Hz in order to avoid downstream signal processing problems, so it doesn’t properly represent either signal or noise at those low frequencies.

In particular, any *DC offsets*¹ have no significance.”

These comments highlight an issue facing any attempt to detect and characterize memory effects. A truly constant component of strain is not meaningful for a gravitational wave interferometer, which senses only changes. However the footprint of GW memory – two intervals (“before” and “after”)

¹ There is considerable confusion in the use of this term, both generally and in the context of GW memory. In many settings, such as a constant signal in the presence of a sinusoidal (AC) component, the “DC offset” is the difference between the constant and the mean value of the sinusoid, zero, or some other fiducial value. Even the more appropriate term *quasi-direct current behavior* used by Zhao, Liu, Cao and He (2021) does not fully capture the reality of memory. Setting semantics aside, here the term *offset* refers to the size of the relatively sudden strain change at the time of a merger event – from a constant before to a constant afterward – and should not be confused with other terminology.

of different but constant strain, separated by an interval ("during") of relatively rapid change – is quite different from a pure constant. This signal contains both low and moderately high frequency variability.

Toward understanding this issue more quantitatively, Figure 1 depicts relevant time series and amplitude spectra of models for the nominal memory effect for the Hanford data for GW 150914. The top panel shows theoretical curves for the chirp, or non-memory, signal plus several simplified models for the corresponding memory build-up. In both panels three broken lines refer to different choices for the parameter – the coefficient in the argument of the hyperbolic tangent function – that determines the speed of the memory build-up. The bottom panel depicts corresponding spectra (amplitude spectra, as opposed to power spectra, are relevant for gravitational waves). In addition to spectra for the three continuous memory models, this plot includes one for a discontinuous template, with a gap during the interval of the main chirp signal, computed with an algorithm for the complex Fourier transform of arbitrarily spaced data [Scargle \(1989\)](#), equivalent to the square-root of the Lomb-Scargle periodogram ([Lomb 1976](#); [Scargle 1982](#)).

As expected from the long time scales associated with the step-function shape, the memory spectra have their strongest contributions at low frequencies. Nevertheless the relatively rapid jump yields significant contributions at somewhat higher frequencies. In the spectrum of a discontinuous jump, separated by a gap in which no data are presented to the algorithm (solid black line) – perhaps most relevant to the analysis presented in §3.2 – these frequencies are somewhat further attenuated. There is considerable overlap of the important bandpasses for chirp and memory signals, but with memory leaning somewhat toward lower frequencies. This has long been understood. For example [Braginsky and Thorne \(1987\)](#) and [Thorne \(1992\)](#) noted that memory detection should be optimal in the frequency range designed for maximum interferometer sensitivity to non-memory signals.

In summary, information below 8 Hz is not available, so of course the analysis here makes no use of this frequency range. However the spectrum of the memory signal contains considerable amplitude above this cutoff – especially between 10 Hz and 30 Hz, but continuing to frequencies as high as 60 Hz or so. Any detection of memory effects must be in spite of the unavailability of very low frequency information, due to unavoidable instrumental and data analysis attenuation of long timescale variability and its suppression in the public data.

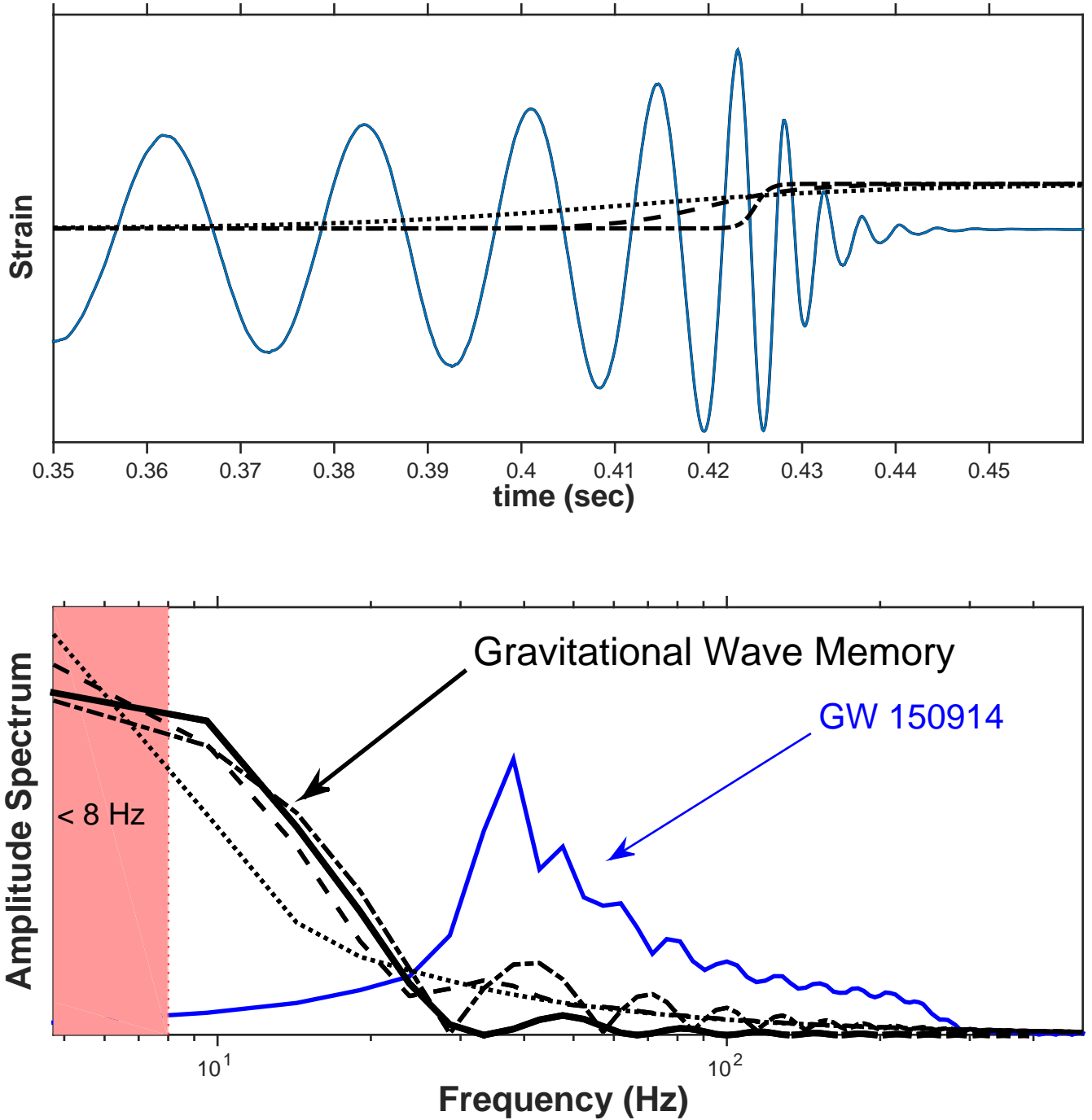


Figure 1. **Top:** Theoretical strain curves; the numerical relativity strain for GW 150914 (Gravitational Wave Open Science Center 2020) (solid line), and hyperbolic tangent curves serving as simplified models of the memory effect (Favata 2010) in various line styles are for three values of the model parameter determining the rapidity of the memory build up. **Bottom:** Linear plots of amplitude spectra (logarithmic frequency scale) derived from the theoretical time series in the top panel. The amplitude units are arbitrary, but the relative normalization is correct for the assumption that the memory offset is 25% of the maximum of the strain in the chirp signal, as in the example in (Favata 2010). The thick solid curve is the amplitude of the Fourier transform of a template with zero strain before 0.38 seconds, followed by a .05 second gap devoid of data, with unit strain after 0.43 seconds.

1.3. Measuring the Permanent Strain Offset

The difficult problem of detecting memory effects is alleviated because they occur at the same time as known merger events and are not necessarily weak² compared to them. Furthermore the approach adopted here avoids difficulties facing much previous work, discussed in §4.3, because it does not depend on the details of the development of the memory signal. What is measured is only the final strain offset: the average strain after the chirp merger signal minus the average strain before it (thus ignoring the chirp itself).

As discussed in §3.4 statistical significance is assessed by applying the same estimation procedure to time-shifted data, much as is standard in detection of mergers themselves. Data *during* the merger events serve only one purpose here, namely demarcation of intervals for averaging the pre- and post-event strains. (However they play a role in the relative offsets defined in Equation 4 and displayed in Figure 3.)

The next two sections describe the major data analysis elements: the quotidian but crucial denoising the raw data, and measuring strain offsets, with results presented in §3.3.

2. DATA SELECTION AND PRE-PROCESSING

Strain time series, sampled at 16 kHz over intervals of 4096 seconds approximately centered on the merger events, were downloaded from the GWOSC site (Abbott et al. 2021; Gravitational Wave Open Science Center 2020) as constituted in July of 2021. Here and throughout, the term *merger event* refers to the chirp signal beginning at a designated time somewhere in the *inspiral* phase and ending at the end of *ring-down* – i.e. adjacent to but excluding the intervals selected for pre-event and post-event strain averaging. These pre- and post- intervals are determined from the GWOSC time-frequency distributions as described in §2.1. The individual data series (here called *observations*) from Hanford, Livingston or Virgo, with missing data or for events flagged as marginal, were generally omitted. GW 191223 and 191225 were included due to their remarkable time-frequency patterns, but in GWOSC documentation are now deemed likely to be glitches. The following processing steps are described in order of their application.

2.1. Data Selection

In total 67 observations (28 from Hanford, 35 from Livingston, and 4 from Virgo) from 41 different black hole mergers, were selected for analysis. Strain offset estimation by subtracting pre-event from post-event strain requires scrupulous avoidance of the potentially confounding contribution from the event itself. Therefore only those cases were included where the effective beginning and end of the merger signal can be reliably estimated from time-frequency distributions displayed at the Gravitational Wave Open Science Center (2020).

Carefully estimated first and last appearances of the oscillatory “chirp” signal mark the event beginning and ending times, in order to define the pre-event and post-event averaging intervals utilized in §3.1. In those few cases where the temporal extent of the visible signal was ambiguous, e.g. due to low signal-to-noise in the leading and trailing parts of the time-profile, the conservative choice was made to minimize any possible leakage of non-memory signal by slightly overestimating the event’s extent. Since the initially sinusoidal inspiral does not have a distinct beginning, and even the rapidly decaying ringdown has a slightly indistinct end, the goal is to estimate two times: when the memory signal has significantly (1) risen above its constant pre-event value, and (2) approaches its constant post-event value. Small errors here yield less potentially confounding non-memory contribution than one might think; a nearly sinusoidal strain averages to approximately zero, as long as one or more

² E.g. the predicted memory offset is 25% of the maximum non-memory strain in the Figures in Favata (2009, 2010).

cycles are included. This cancellation was enhanced by slightly shifting the selected times away from the merger chirp to the nearest zero-crossing, thus approximating nodes of the noise oscillations (details are given in Appendix D).

The remaining steps slightly adapt standard pre-processing methods (e.g. [Abbott et al. 2020](#), cf. Fig. 3) to the present purpose of detecting non-oscillatory strain. After ensuring zero-mean and convenient normalization of the full time series, the following steps were applied.

2.2. Centering the Merger Events

In the public data files the center of the merger differs slightly from the midpoint of the data interval, typically by a fraction of a second. This actually has a small but measurable effect on the results. With tapering symmetric about the midpoint, an offset signal would occur on a sloping part of the taper, yielding a potential bias that could masquerade as a memory effect. Hence the time series were shifted to bring the mean of the event beginning and ending times to the center of the analyzed interval, as described in Appendix C. Two treatments of the resulting end effect yielded negligible differences: auto-regressive extrapolation into the small interval shifted out of range, and truncation (by 2 seconds); the results presented here use the former.

2.3. Whitening

To suppress the strong, correlated, and highly non-normal noise in strain data, while retaining as much gravitational wave signal as possible, whitening of the raw time series is crucial. The time series were transformed to make their power spectra nearly independent of frequency, using the formula

$$h_{\text{white}}(t) = \text{IFFT} \left\{ \frac{\text{FFT}[w(t)h(t)]}{S(\omega)} \right\} . \quad (1)$$

Here $h(t)$ is the raw strain, $w(t)$ is a window function called a *taper*, and FFT and IFFT are the fast Fourier transform and its inverse. The denominator $S(\omega)$, in a rough sense essentially the absolute value of the numerator, was evaluated in three ways: directly and – in the spirit of Welch power spectrum estimators – using (tapered) block-averages with and without overlap. The direct approach fully divides out the amplitude spectrum, leaving only the phase spectrum. Block averages were implemented using somewhat standard 4-second blocks and, when used, 2-second overlap.

The importance of tapering to control phase modulations and spectral leakage in these Fourier transforms has been emphasized in many publications and GWOSC tutorials. From among the dozens of windows in common use³ most GW analyses have chosen the classic Tukey taper or alternatives ([McKechan, Robinson and Sathyaprakash 2010](#)), with little or no explicit justification for the choice. It is often thought that there is no unique, favored, all-purpose windowing method. However [Thomson \(1982\)](#) rigorously derived tapers that explicitly minimize spectral leakage over all possible window shapes. The resulting *multi-tapers* are a family of eigenfunctions (discrete prolate spheroidal wave functions, traditionally called Slepians) maximizing the power contained in the main lobe of the spectral response function ([Slepian 1978](#); [Thomson 1982](#); [Percival and Walden 1993](#)). Besides reducing variance, the higher order tapers emphasize the ends of the data interval, thereby recovering information degraded by standard tapers. (Of course here this feature is less important for the well-centered events, but might be useful e.g. in searching for bursts occurring anywhere in the interval.)

Four tapers schemes were evaluated: Tukey, zero-order Slepian, a combination of zero-order and first-order Slepians, and a combination of zero- first- and second-order Slepians. (The combinations

³ Such tapers are mostly ad hoc guesses for what might make a good spectral window. With a very few exceptions, such as Dolph-Chebyshev, the proposed windows are not generated from an unambiguous quantitative principle, as are the Thomson tapers.

were implemented by averaging the whitened time series, not by whitening the averaged time series.) Since taper symmetry is important for the same reasons discussed with regard to centering in §2.2, the first order Slepian, which is antisymmetric, was applied in both direct and time-reversed form. Details are given in Appendix E. The procedure described in §3.3 determined the optimum whitening procedure. among the 12 combinations of four tapers and three variants of Equation (1), separately for each observation. As can be seen from Table 1 multi-tapering often outperforms the Tukey taper.

2.4. Bandpass Filtering

In principle the variability timescale of a *permanent* strain offset is unlimited on the long end, extending down to timescales of the rapid memory buildup during the merger on the short end. Other considerations aside, then, the nominal frequency range in the present context is $10^{-4} - 10^3$ Hz, for timescales from the full observation interval of 4096 seconds to a few milliseconds. However several considerations cannot be set aside (cf. §1.2). Rapid increase in seismic noise below 10 Hz, filtering of the public GWOSC data below 8 Hz, and declining instrumental response at these frequencies are all realities that weigh heavily on memory detection efforts. The discussion in §1.2 drove the choice of bandpass filtering of all observations between 20 Hz and 200 Hz⁴, implemented with the Matlab finite impulse response bandpass filter of order 2048.

2.5. Optimal Cleaning

The 12 possible cleaning procedures described above (4 tapers \times 3 whitening schemes) were optimized by maximizing the resulting signal-to-noise for each of the 67 events:

$$\text{Signal-to-Noise} = \frac{\text{Recovered Event Amplitude}}{\text{Noise Standard Deviation}} \quad (2)$$

The numerator is the measured absolute range during the event. The denominator is the mean of standard deviations of the residual noise, computed over four intervals of length Δ bracketing but not including the event: two before and two after the event, offset from it by Δ and 4Δ . The value used for Δ was the duration of the merger event.

The resulting optimum cleaning methods and their parameters varied widely from observation to observation (cf. the “code” entry in Table 1). No choice could be singled out as generally best. This situation is probably due to marked inhomogeneity, invisible in strain time series plots, of the character of the noise: unusual, non-stationary and non-Gaussian behavior. Hence the need to optimally adapt the tapers and whitening methods to the vagaries of the noise, by maximizing the signal-to-noise for each individual observation.

2.6. Strain Calibration

The cleaning procedure outlined in the previous section introduces various scale factors into the final whitened and filtered strain. It is desirable to remove these somewhat arbitrary factors to yield calibrated strain time series. This was accomplished by analyzing in the same way two data series – each consisting of the raw data for the given observation – one with test signals of known amplitudes inserted at two locations, a second before and a second after the time of the merger event, and one without. The difference between these two cleaned time series was then compared to the inserted signal to determine a calibration constant for that observation. These calibration constants were found to be nearly independent of the shape of the injected test signal, and the results shown here are based on a descending linear ramp of width equal to the duration of the merger chirp signal.

⁴ Filter parameters optimized using the technique in §2.5 were explored, and gave slightly smaller strain offset estimates and slightly larger uncertainties. This procedure does not explicitly respect the issues addressed in Figure 1, and was not pursued.

The strain offset estimates were evaluated in two forms: calibrated in this way (calibrated “absolute” strains) and normalized by the maximum of the absolute value of the strain during the merger (self-calibrated “relative” strains, cf. Fig. 3).

3. MEASURING THE STRAIN OFFSET

We are now ready to measure the strain offset from the cleaned time series. After defining the intervals over which to average the pre- and post-event strains, several averaging methods are considered.

3.1. Pre-Event and Post-Event Averaging Intervals

Braginsky and Thorne (1987) emphasized that lengths of averaging intervals are crucial for detection of memory effects. Expanding on this point, Figure 2 shows the response of a sample pre-processing procedure to the addition of the simple hyperbolic-tangent memory expression⁵ mentioned in §1.2. Of crucial importance is *the decay of the post-event strain offset on a time scale roughly the same as the duration of the merger event itself*. This decay toward zero – herein called *reversion* – is a result of the pre-processing procedure as a whole. (Figures 1 and 2 of Ebersold and Tiwari (2020) depict similar considerations in both the time and time-frequency domains.) Since this effect is the result of time-symmetric processing operations, it is not causal and should affect both the pre-event and post-event strain equally. Additional reversion will arise from the interferometric detector system’s response, not included in this figure. This second effect is causal, so the combined reversion will be stronger after the mergers than before – suggesting that the post-event averaging interval should be shorter than the pre-event one. (Note the small downward shift in the pre-event strain and the preservation of its detailed structure. The pre-event averages will automatically incorporate this shift.)

In principle, in estimating the “permanent” strain offset predicted by theory, one would like to average over an infinite length of time. In reality it is necessary to take account of the reversion of the observable memory signal due to instrumental and data analysis effects. The considerations above led to the adoption of pre- and post- merger averaging intervals 8 and 0.75 times the duration of the main part of the merger chirp signal as defined in 2.1.

3.2. Averaging Methods

The median was adopted to measure strains in the pre-event intervals due to its well-known *robustness* (Claerbout and Muir 1973), i.e. insensitivity to outliers. Two estimators of the average strain during the post-merger interval $t_1 \leq t \leq t_2$, where t_1 and t_2 are the endpoints of that interval as defined in §3.1, were considered: a weighted mean emphasizing earlier times via the weight function $w(t) = (t_2 - t)/(t_2 - t_1)$, and a linear fit to the strain, evaluated at $t = t_1$. These metrics explicitly target the post-event reversion demonstrated in Fig. (2). The resulting estimate of the *strain offset* is defined as the difference in strain averaged over the pre- and post- intervals:

$$\text{Strain Offset} \equiv h(\text{post-event}) - h(\text{pre-event}) = \Delta h_{\text{mem}} \quad . \quad (3)$$

Also of interest is the relative strain offset – i.e. the strain offset defined above divided by the maximum absolute value of the strain during the event:

$$\text{Relative Strain Offset} \equiv \frac{h(\text{post-event}) - h(\text{pre-event})}{h_{\text{max}}} = \frac{\Delta h_{\text{mem}}}{h_{\text{max}}} \quad . \quad (4)$$

⁵ Other than its use here in motivating averaging choices, this toy model is not used in the analysis.

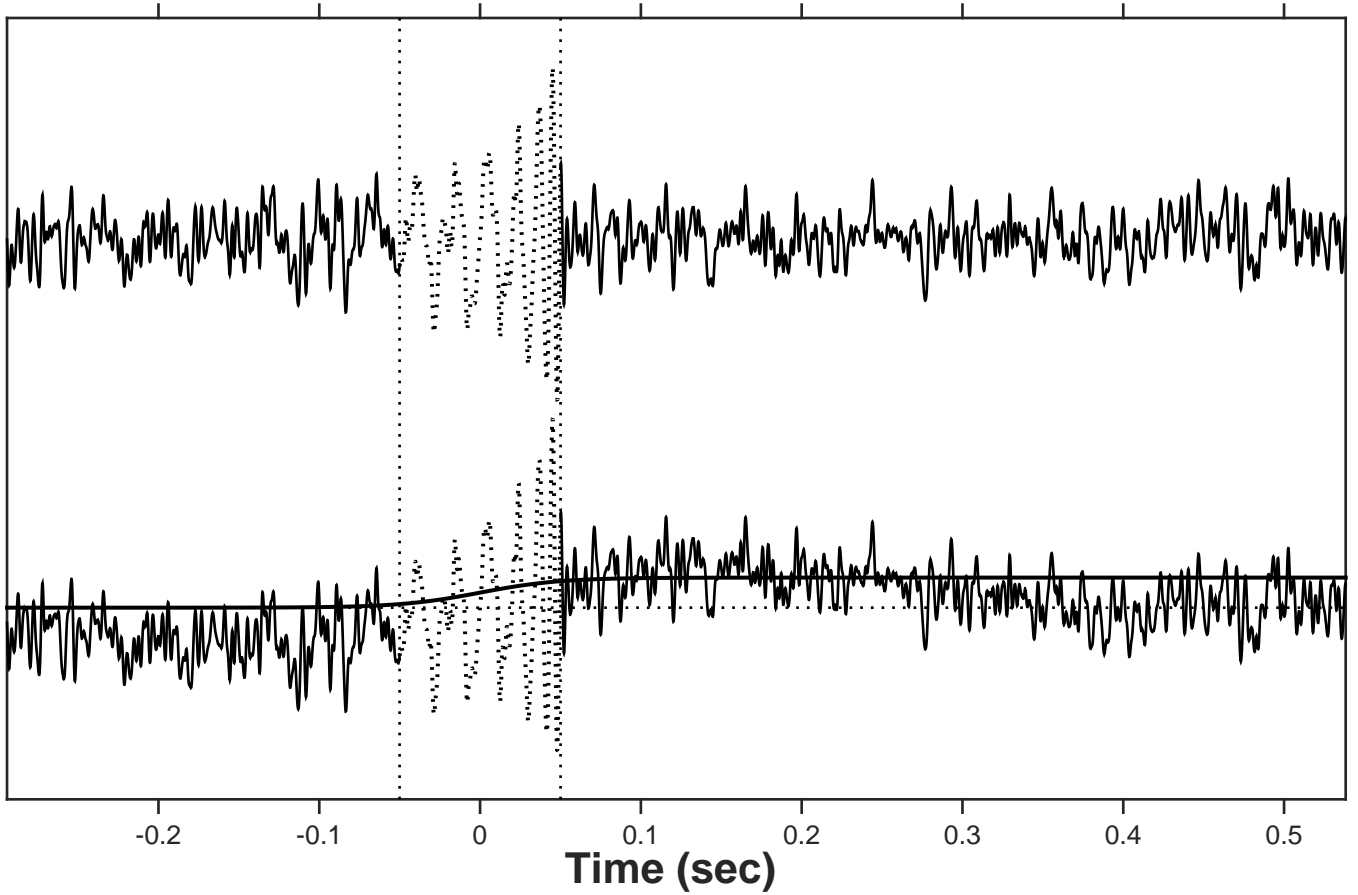


Figure 2. Top: Hanford strain data for GW 150914, centered, whitened using a zero-order Slepian taper, and low pass filtered at 200 Hz; amplitude scale arbitrary. Bottom: A *hyperbolic tangent* step function (smooth solid line) has been added to the same input data as in the top panel, and processed in the same way.

This convenient scaling provides a reliable self-calibration. It might be thought that the antenna pattern, a coefficient dependent on the relative orientation of the observer and the merging black hole system, would cancel out in this expression. However the antenna pattern depends also on polarization, which is generally different for the memory and non-memory signals, yielding different effective antenna patterns. A straightforward evaluation of the angular dependence of the corresponding antenna pattern factors in the numerator and denominator of Equation (4) shows that, while that there is approximate cancellation over a moderate range of source-detector geometries, cancellation of these factors cannot be relied on. The theoretical results of Zhao, Liu, Cao and He (2021) – and the supplementary data provided by these authors and used to construct Figures 5 and 6 here – include a proper evaluation of the full antenna patterns for the individual merger events.

3.3. Results

Appendix A tabulates estimates of the strain offsets, calibrated but not corrected for instrumental sensitivity, with uncertainties as determined below in §3.4. Results with two estimators for the post-event strain are exhibited to highlight a moderate dependence on averaging method, presumably due to different responses to noise fluctuations. Figure 3 plots, in the upper panel, the relative offsets of Equation (4), which are self-calibrated and thus do not rely on the absolute calibration described in

§ 2.6. The bottom panel depicts signed normal scores (sometimes called standard scores) ranging in absolute value from < 1 (indicating upper limits) to ~ 3 – i.e. detections with the corresponding

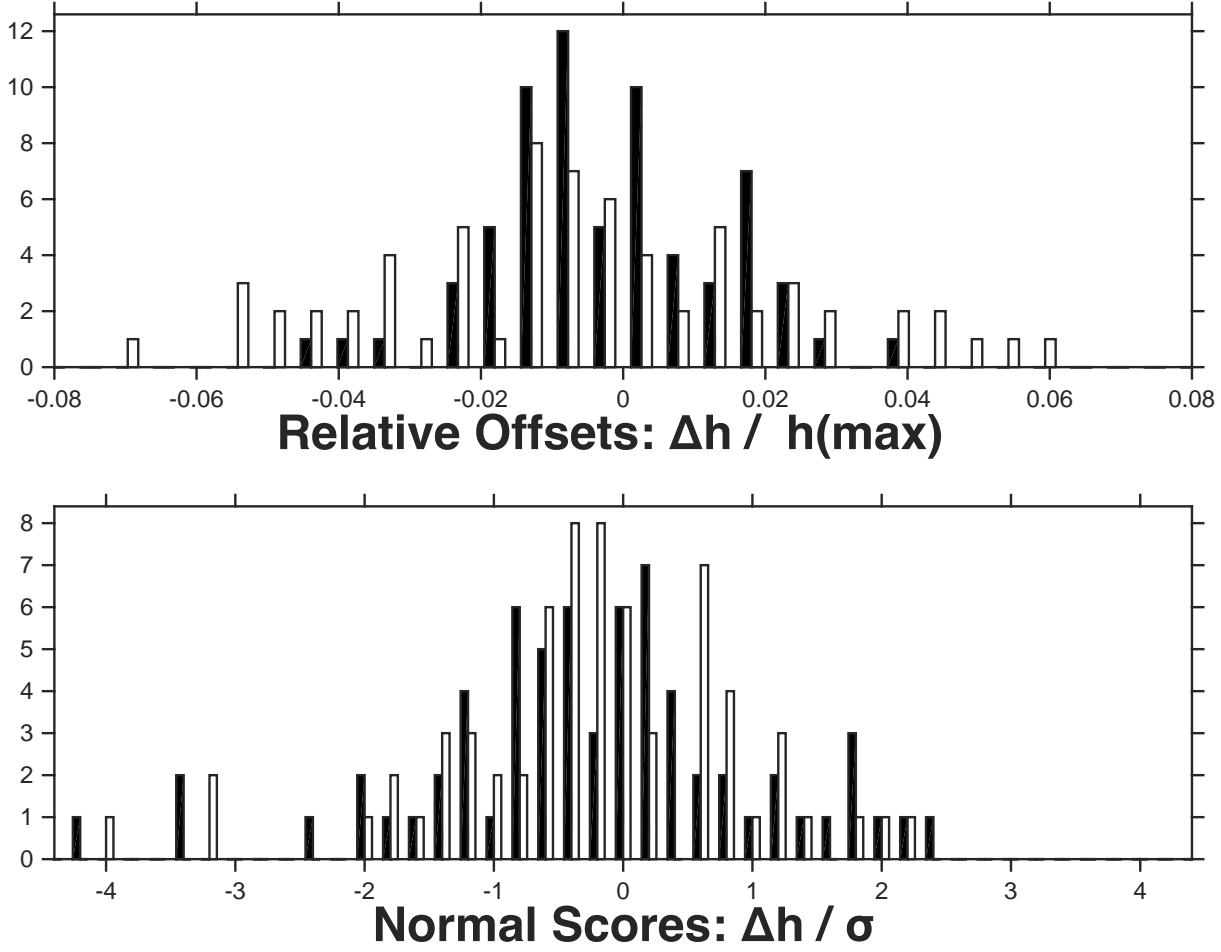


Figure 3. Histograms of the 67 strain offset estimates obtained with 2 metrics (black = weighted mean; white = linear fit). Top: Relative strain offset, Δh_{mem} divided by the maximal absolute value of the strain during the merger event, as in Equation 4. Bottom: signed *normal scores* (also known as *z-scores*): Δh_{mem} divided by the standard deviation from the time-shift analysis described in §3.4.

Figure 4 depicts the 12 events with the greatest absolute standard errors and with reversion toward – not away from – the mean. Each panel indicates the part of the pre-event averaging intervals, and all of the post-event averaging intervals. The red vertical bars indicate the $1\text{-}\sigma$ error value determined for the linear fit metric described in § 3.2.

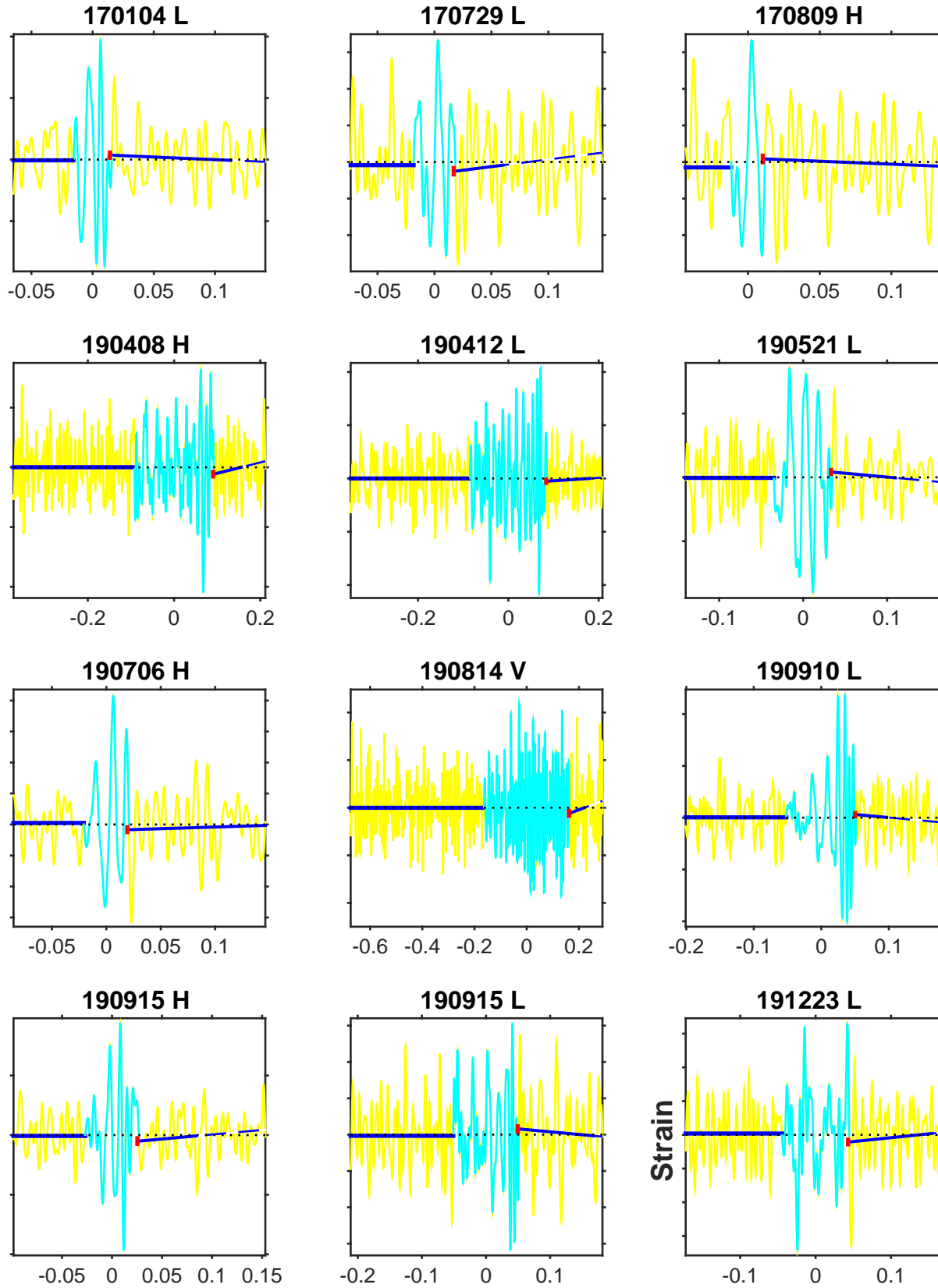


Figure 4. Cleaned strain time series (solid yellow lines, cyan during the event). The median pre-event strain is plotted as a thick solid blue line; the linear fit to the post-event strain is a thinner line, switching to dashed if and when it crosses the pre-event level. These are the 12 observations with the largest standard scores and also with linear fit slopes indicative of reversion to zero (cf. property (a) discussed in §4.2). Red error bars are the uncertainties in the linear fit values, obtained from the time-shifted data.

3.4. Statistical Significance

Statistical uncertainties were assessed in a way similar to that commonly used to estimate false detection rates for mergers. Data time-shifted in half-second steps, covering the 1024 seconds centered on the event (i.e. $\frac{1}{4}$ of the full 4096 seconds, but skipping one on either side of the event), were analyzed in exactly the same way as the non-shifted data. This is much like scanning the data with a template consisting of the before and after intervals separated by a gap at the merger event. The main difference from standard templates-based searches is that the time of the event is known a priori. Here scans are used in a different way, namely to calibrate the response of the template to the noise well before and after the event. In particular, random errors are quantified using the standard deviations of the resulting set of 2046 strain offsets measured in the shifted data, and shown as 1σ standard scores (also known as normal scores) in Figure 3 and Table 1. It is straightforward to estimate confidence intervals, directly from the shifted data, without assuming the errors are normally distributed; these did not differ significantly from the standard deviations and are not reported here.

It is less straightforward to assess the aggregate statistical significance of an ensemble of measurements. The underlying question is: how likely is the set of obtained standard scores to arise by chance, given the noise in the data? The answer to this probabilistic question depends on the adopted criterion for the success of realizations of the process consisting of random samples from the error distribution. This task is complicated by the fact that the outcome of a realization is an array of 67 standard scores, not just a single parameter. An example of a convenient statistic is the number of observations where the absolute value of the standard score exceeds a specific value – e.g. the number of detections at 3σ or greater. A straightforward simulation consisting of 1M randomly shuffled draws from the time-shifted data shows that the probability that number of standard scores that equal or exceed the actual value, which is 3 for both cases, is .0030 for the weighted metric, and .0005 for the linear fits. Of course there is danger in treating a specific result found in data (a posteriori) as though it were pre-selected (a priori) as the only result that would have been of interest. But this criterion, based on the number of individual observations at or above a standard significance level, is relatively generic. Hence these numbers are approximate measures of the false positive rate, where “positive” means three or more standard scores $\geq 3\sigma$.

4. DISCUSSION

Detection significances derived from a straightforward time-shift analysis are not the whole story. This section first describes features unlikely under the null hypothesis (mere statistical fluctuations), which taken together add credibility to the claim of detection of memory effects. There follows some comparisons with theoretical expectations and a discussion of possible future improvements.

4.1. Hanford-Livingston Comparison

A check on the validity of any detection of memory (or of non-memory signals, for that matter) resides in consistency of the results using data from different observatories. For a given event, after accounting for the differing instrumental response (“antenna pattern”), the estimated strain should be the same within the uncertainty set by residual observational noise. Even for non-memory signals this consistency is typically examined from independent analyses of data series from different observatories (and not using a joint model fitting procedure). This is the approach adopted here. Figure 5 explores correlations between offsets measured and calibrated from Hanford and Livingston data for the 22 events where both observations passed the selection criteria of §2.1. Since observed strain is true strain modified by instrumental sensitivity, ideally the corrected strains should satisfy:

$$\text{Estimated } h(\text{True}) = \frac{h(\text{observed, Hanford})}{A(\text{Hanford})} = \frac{h(\text{observed, Livingston})}{A(\text{Livingston})}, \quad (5)$$

where A denotes the instrumental response, or antenna pattern. Accordingly the plotted Livingston values $\hat{h}(\text{Livingston})$ are adjusted using

$$\hat{h}(\text{Livingston}) \equiv E\left[\frac{A(\text{Hanford})}{A(\text{Livingston})} \right] h(\text{Livingston}) \quad (6)$$

This relation was implemented using numerical data kindly provided by Zhao and Cao (cf. [Zhao, Liu, Cao and He 2021](#)), taking into account that the polarization of memory is very accurately ”+” only. $E[]$ refers to these authors’ estimation procedure for the ratio. As can be seen in their plots of posterior distributions, the resulting estimates have rather large uncertainties. The correction factor is a random variable, estimated using values of source parameters (black hole masses, orbital orientations, etc.) which in turn are random variables derived from the raw observations, with considerable uncertainties of their own. The form in Equation (6) was found to be relatively robust, presumably due to partial cancellation of the parts of the antenna patterns dependent on source parameters (including the orbital orientation), which are of course common between different observatories. These adjusted values are plotted as open circles; for comparison, the intersections of the x- and y- error bars are the Livingston values adjusted by the simple sign flip that captures the lion’s share of the relative instrument sensitivity between Livingston and Hanford ([Abbott et al. 2016](#), the caption of Fig. 1). Note the rather small differences between these values.

The error bars themselves express the uncertainties discussed in section 3.4. (Separate error bars for the open circles are not shown, but would be slightly larger due to the added uncertainty of the antenna pattern correction discussed above.)

The famously strong initial event GW150914 seems to be something of an outlier in both panels, so regression parameters were computed both with and without this point, with results as detailed in the caption and notations in the plot. The overall conclusion to be drawn from these scatter plots is that – in spite of rather large uncertainties – there is modest evidence of correlations between the memory measurements from these two observatories. For the linear-fit metric (right-hand panel), with GW 150914 excluded, the p-values for both instrumental sensitivity adjustments are on the order of .01. On the other hand, the fact that the slopes of the regression lines are systematically and significantly less than unity is not consistent with what is expected – possibly due to an unappreciated systematic error in the measurements or their adjustments. Accordingly these results should be taken as a moderately weak confirmation of the physical reality of the measured memory offsets.

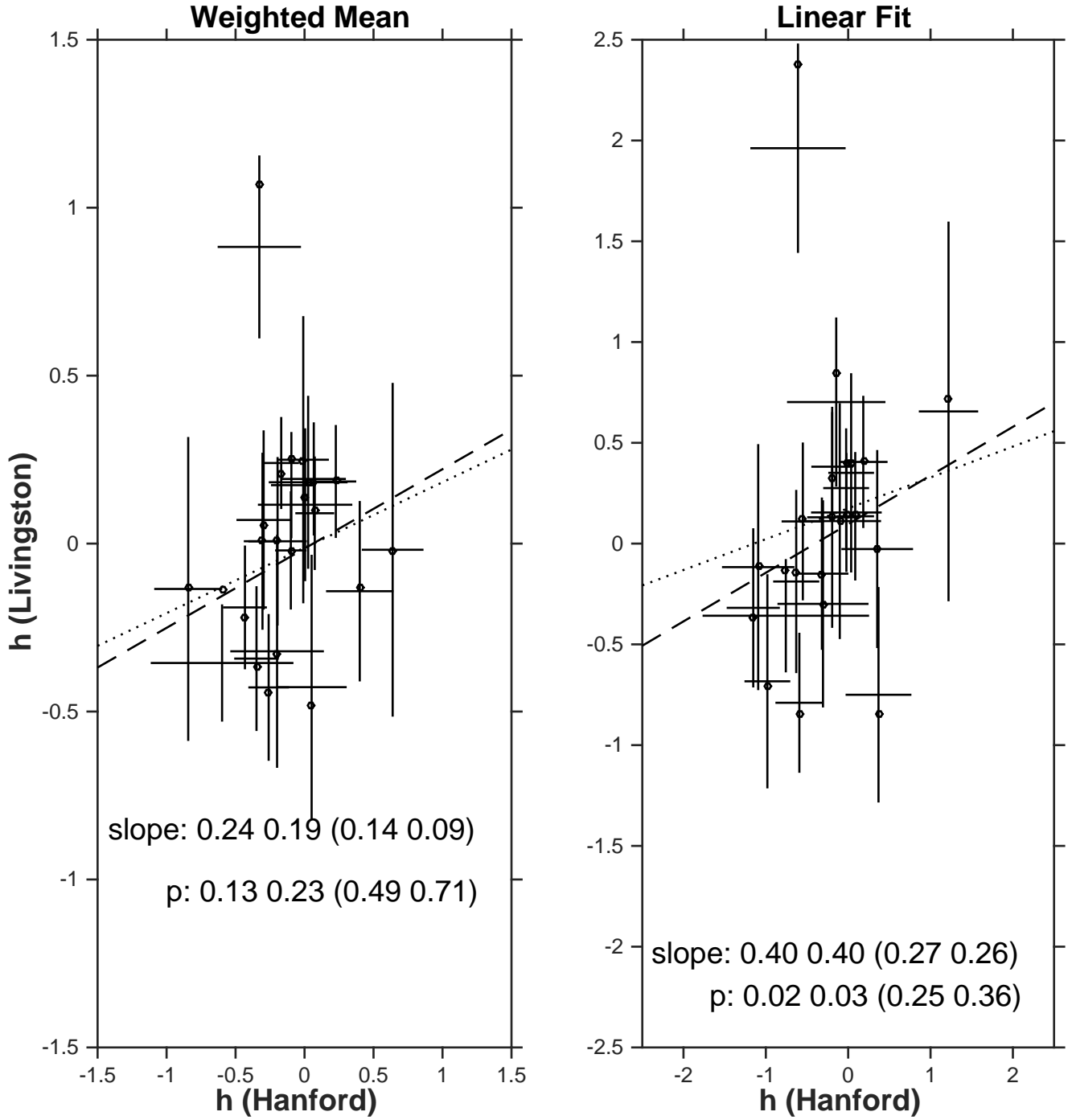


Figure 5. Scatter plot of the measured strain offsets for the 22 events where both Hanford and Livingston observations passed the selection criteria in §2.1. These calibrated strain offsets are scaled relative to 10^{-22} . The Livingston values plotted as open circles are adjusted for the relative instrumental sensitivity between the two observatories using Equation (6). Their regression lines are shown as dotted and dashed lines, with and without the outlier point (GW 150914, which has the largest Livingston values) respectively. The intersections of the x- and y- error bars indicate the values adjusted with the simple "sign-flip." Indicated regression slopes and significances – i.e. Pearson probabilities for accepting the null hypothesis of no correlation – are for these two adjustments (sign flip, full antenna pattern) respectively, with the outlier point excluded. (Values in parentheses are with the outlier included.)

4.2. Preponderance of Reversion over Divergence

A linear fit represents either (a) reversion to, or (b) growth away from, pre-event strain levels. There are in fact 57 cases of (a) and only 10 of (b). Taking these as equally likely in random noise, the formal probability of this or a more extreme imbalance is $\sim 10^{-10}$.

4.3. Previous Studies of Memory Observables

For several decades, in parallel with the theoretical work mentioned in § 1.1, numerous authors have studied GW memory observables (Kennefick 1994; Lasky et al. 2016; Talbot, Thrane, Lasky and Lin 2018; Yang and Martynov 2018; Johnson et al 2019; Boersma, Nichols and Schmidt 2020; Ebersold and Tiwari 2020; Hübner, Lasky and Thrane 2020, 2021; Khera, Krishnan, Ashtekar and De Lorenzo 2021; Zhao, Liu, Cao and He 2021), with the aim of establishing reasonable prospects for detecting and characterizing the effects.

Kennefick (1994), based on considerations similar to those in §1.2, notes that the spectrum of the memory growth signal is reasonably well matched to the (planned at that time) LIGO and VIRGO broadband gravitational-wave detectors’ optimal performance at around 100 Hz, hence well suited to detect “the growth of the memory amidst the chirp.” Further, in mergers involving a neutron star, memory effects originating during its tidal disruption could yield estimates of the neutron star’s radius. However, this author considers marginal any prospects for detecting even the larger memory effects in BH-BH mergers.

Two publications (Lasky et al. 2016; Talbot, Thrane, Lasky and Lin 2018) discussed the importance of higher-order gravitational-wave modes for determining parameters of binary black hole mergers. The former authors estimate that approximately 100 events with masses and distances similar to those of GW150914 will be needed to achieve memory detection with a signal-to-noise ratio of 5. Similar pessimistic conclusions, based on the statistics of co-analysis of many events, echo throughout most of the subsequent research now to be discussed. For example (Yang and Martynov 2018) conclude that elucidation of the angular distribution of memory, deemed difficult for Advanced LIGO/Virgo, will be possible with a future third-generation detector network. Similarly Johnson et al (2019) conclude that current ground based detectors are unlikely to detect nonlinear memory “without a clever stacking scheme as in ...” (Lasky et al. 2016; Yang and Martynov 2018).

Boersma, Nichols and Schmidt (2020) conclude that evidence for the GW memory effect will probably be found within a population of a hundred or so binary black hole mergers sooner than in individual mergers – except possibly in an event significantly stronger than any heretofore detected. Specifically they estimate five years of data collected by LIGO and VIRGO will yield a signal-to-noise ratio of about 3. These authors also pointed out that “the different approximation methods used to compute the GW memory effect can lead to notably different signal-to-noise ratios,” another conclusion pervading the literature.

Ebersold and Tiwari (2020) performed an unsuccessful search of part of the O2 Hanford-Livingston data release for memory signals from mergers of black holes of less than a solar mass. Their approach, quite different from that described here, involved a blind search (since for such masses the non-memory component is at frequencies too high to be detected by LIGO) using the coherent WaveBurst algorithm in the time-frequency domain.

More recent work has addressed measurement specifics. Hübner, Lasky and Thrane (2020, 2021) developed a Bayesian detection framework and applied it to black hole mergers in LIGO/Virgo’s gravitational-wave transient catalogs – 10 events from GWTC-1 in the first paper, and 50 from both GWTC-1 and GWTC-2 in the second. The odds ratios for models with and without memory are less than 1.015 for the first 10 events and less than about 1.025 for all 50; the combined Bayes factors were

no more significant. Based on both studies these authors suggest that an ensemble of 2000 binary black hole observations will be needed before definitive evidence for gravitational-wave memory will be practical.

In the broader setting of tests of non-linear general relativity [Khera, Krishnan, Ashtekar and De Lorenzo \(2021\)](#) treat the total gravitational memory as an inferred observable, on the same footing as the mass and the spin of the final black hole. The emphasis of this work was to assess memory predictions based on two different candidate theoretical merger waveforms: Phenomenological and Effective-OneBody. That is, they explored the use of agreement between the posterior distributions of various angular modes of total memory as diagnostic tools to further improve the non-memory waveforms. For a sample of 10 GWTC-1 events they found generally good agreement between the corresponding memory posterior distributions, but with discrepancies in the $l = 2, m = 1$ mode, and lesser ones for $l = 4, m = 0$ suggesting possible sources of systematic errors not captured by the posterior distributions of other inferred observables.

In summary, the work discussed so far, yielding neither memory detections nor upper limits, is pervaded by two themes pessimistic with regard to near-term prospects: (1) the need for a much larger ensemble of events than currently available, and (2) the fact that current theoretical memory estimates have significant dependence on assumptions, approximation schemes, and uncertain merger parameters. All analyses of the kinds described above face considerable difficulties through the need for accurate models and parameters – masses, spins, and orientations. The relevant numerical relativity effort – intensive on-going research using various approximation schemes – is not a settled activity. Furthermore *mixture model* problems have inherent solution uniqueness issues that can make them nearly ill-posed ([Acton 1990](#)).

Recent work by [Zhao, Liu, Cao and He \(2021\)](#) marks an improvement of this situation and allows rather direct comparison of the results presented here and theoretical predictions. These authors introduce a novel scheme to estimate GW memory for a binary black hole (BBH) merger, consisting of three parts: (1) a numerical relativity memory simulation using the the Bondi-Metzner-Sachs method; (2) a surrogate model to relate BBH parameters to the memory; (3) use Bayesian techniques to estimate the memory from the surrogate model. In this way GW memory was estimated for 48 GWTC-2 events. Then Kullback-Leibler differences between the resulting posterior and assumed priors distributions, presented in detailed plots, were used to assess the possible presence of memory effects. These authors kindly made their underlying numerical results available, allowing estimation of the observed memory as modified by instrumental sensitivity. Comparison between these theoretical predictions and the values in Table 1 is demonstrated in Figure 5 above, and here in Figure 6. This plot is a direct comparison of the calibrated measurements (not corrected for instrumental sensitivity) with the computed memory offsets adjusted to include the effects of the relevant antenna patterns.

While both sets of values fall in roughly the same range ($\sim 10^{-22}$), this figure provides little evidence of a correlation; however, given the uncertainties in both sets of values it is not inconsistent with a correlation. Definitive contact between observation and theory, while not yet satisfactory, will likely improve in the near future with improved data and analysis techniques.

4.4. Conclusions

Detection of even the simplified signature of gravitational wave memory defined here is difficult. In Figure 4 the putative offsets are largely not obvious in the strain time series; they are small compared

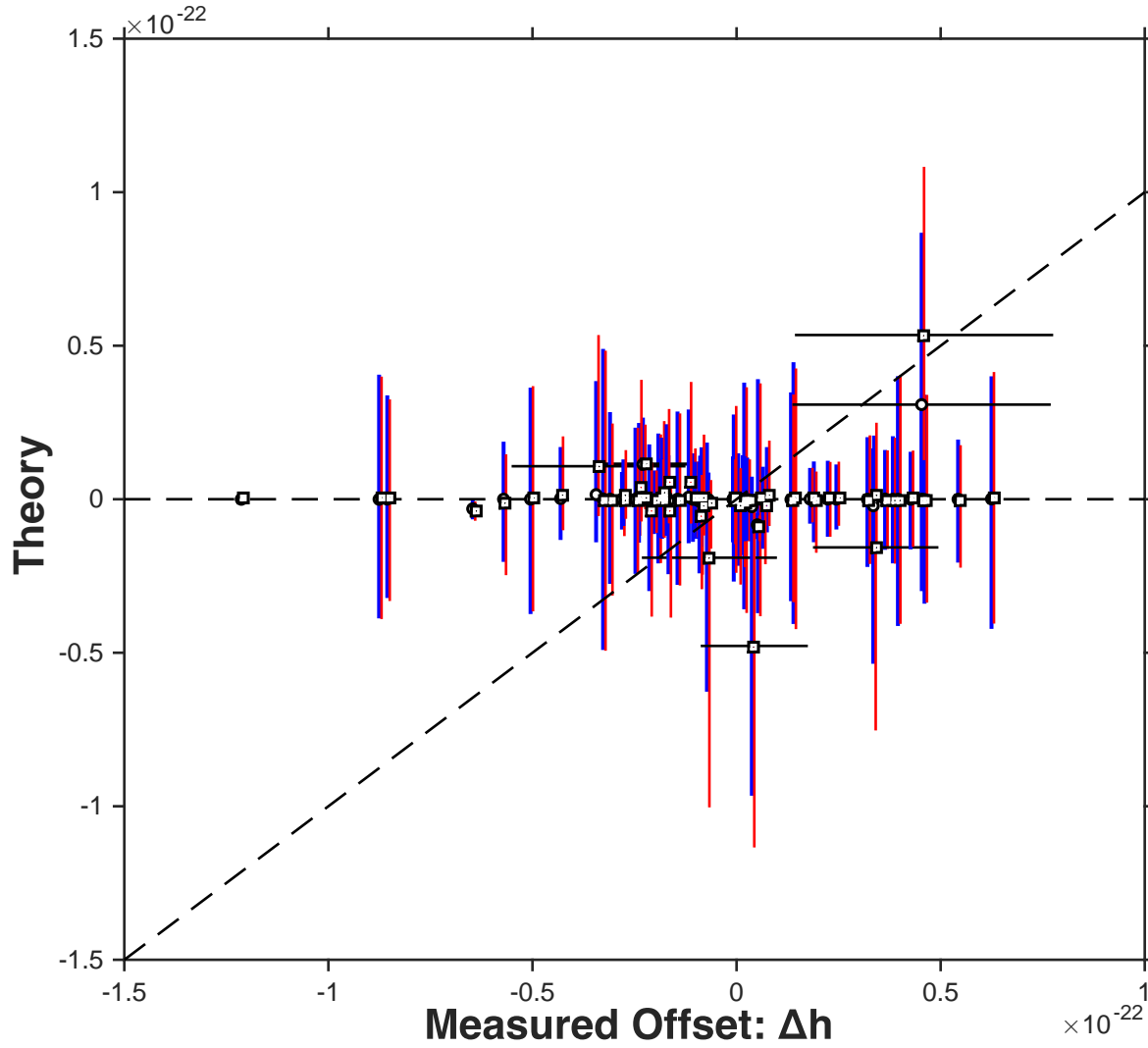


Figure 6. Comparison of predicted and measured strain offsets. Abscissa: strain offsets from Table 1. Statistical errors (dotted lines) are mostly suppressed, as for theoretical values less than ± 0.1 they overlap too much to display. Ordinate: theoretical values at the maxima of the memory posterior distribution functions exhibited in Zhao, Liu, Cao and He (2021) (blue lines) and the posterior median (thinner red lines, offset slightly in the x-direction), with confidence intervals (vertical dotted lines) corresponding to the 5% tails of these posteriors. These values are adjusted to include theoretical estimates of instrumental sensitivity, using additional data privately communicated by these authors, and are thus directly comparable to measurements uncorrected for instrumental sensitivity. Pearson probabilities for accepting the null hypothesis of no correlation are .26 and .65, respectively; linear regression slopes are .017 and .016.

to the surrounding strain variance. While the discussion in the previous parts of this section provide some additional confidence to the statistical analysis of §3, reservation about a claim of definitive detection of memory offsets is justified. In particular, given the various uncertainties encountered in this study, and the lack of definitive comparative cross-checks, the strain offset measurements reported here should be regarded as *probable detections*. Rather definitive confirmation might be achieved if the relative strain offsets were to show a clear dependence on the energy radiated during the merger (cf. Braginsky and Thorne 1987; Favata 2009; Garfinkle 2016). Due to observational uncertainties this test is not yet feasible.

At least two problems have been uncovered by this work. First is the dichotomy between the consensus of the investigations discussed in §4.3 that detection of memory effects with significant

signal-to-noise will require a much larger sample of events (to be combined incoherently), in contrast to the significant detections for a number individual events claimed here. Three cases have standard scores

Second is lack of clear evidence for agreement between the measured values reported here and theoretical predictions, as depicted in Figure 6. The Pearson p-values are not even evidence for a correlation, much less agreement of the values (cf. the tiny slope of the linear regression). Hopefully future reduction of uncertainties in both measured and theoretical values will ultimately resolve these discrepancies.

Even a small signal-to-noise gain through improvements in the data reduction and analysis reported here will no doubt alleviate some of the difficulties. Modifications of the cleaning techniques adopted here could further reduce the random errors that clearly limit these measurements. Examples of avenues for future improvements include: (1) if carried out on shorter intervals, whitening would utilize data closer in time to the events, possibly improving noise reduction; (2) perhaps the most important modification would be use of a more detailed reversion template derived from the instrument and cleaning transfer functions; (3) in the selection of averaging intervals described in §2.1, improvements might follow from basing their definition on objective features of cleaned strain time series, rather than time-frequency distributions; and (4) exploration of currently unknown systematic errors. It is hoped that improvements in modeling and measurement will soon yield definitive tests of nonlinear general relativity based on the memory effect.

I am especially grateful to Zhoujian Cao and Zhi-Chao Zhao for informative comments, and especially for providing numerical data and further computations – used here to generate Figure 6 – underlying the results presented in Zhao, Liu, Cao and He (2021). I am grateful to Bob Wagoner, Ben Farr, Keefe Mitman, and Javier Pascual Granado, for helpful suggestions. Ron Adler, Sasha Buchman, Mike Ely, Gary Godfrey, Neev Khera, Jay Norris, Suraj Poolakkil, Alex Silbergleit, Ron Walton, Suwen Wang, Kent Wood and Paul Worden also provided useful comments. Ben Farr, Alan Weinstein, Brian Lantz and other members of the GWOSC provided useful data help. Many thanks to Joe Bredekamp, the NASA Applied Information Systems Research Program and the NASA Astrophysics Data Analysis Program (Grant NNX16AL02G) for support.

This research has made use of data obtained from the Gravitational Wave Open Science Center (<https://www.gw-openscience.org/>), a service of LIGO Laboratory, the LIGO Scientific Collaboration and the Virgo Collaboration. LIGO Laboratory and Advanced LIGO are funded by the United States National Science Foundation (NSF) as well as the Science and Technology Facilities Council (STFC) of the United Kingdom, the Max-Planck-Society (MPS), and the State of Niedersachsen/Germany for support of the construction of Advanced LIGO and construction and operation of the GEO600 detector. Additional support for Advanced LIGO was provided by the Australian Research Council. Virgo is funded, through the European Gravitational Observatory (EGO), by the French Centre National de Recherche Scientifique (CNRS), the Italian Istituto Nazionale di Fisica Nucleare (INFN) and the Dutch Nikhef, with contributions by institutions from Belgium, Germany, Greece, Hungary, Ireland, Japan, Monaco, Poland, Portugal, Spain.

REFERENCES

- Abbott, R. et al. (LIGO Scientific Collaboration and Virgo Collaboration), 2016, Observation of Gravitational Waves from a Binary Black Hole Merger *Phys. Rev. Lett.* 116, 061102
- Abbott, B. et al. (LIGO Scientific Collaboration and Virgo Collaboration), "A guide to LIGO–Virgo detector noise and extraction of transient gravitational-wave signals," 2020, *Class. Quantum Grav.* 37, 055002 (54pp)
- Abbott, R. et al. (LIGO Scientific Collaboration and Virgo Collaboration), "Open data from the first and second observing runs of Advanced LIGO and Advanced Virgo", *SoftwareX* 13 (2021) 100658.
<https://www.gw-openscience.org/eventapi/html/allevvents/>
- Acton, F. 1990, Numerical Methods that [usually⁶] Work; Interlude: What Not to Compute, p. 253, Mathematical Association of America: Washington
- Bian, L., Cai, R., Cao, S., Cao, Z., Gao, H., Guo, Z., Lee, K., Li, D., Liu, J., Lu, Y., Pi, S., Wang, J., Wang, S., Wang, Y., Yang, T., Yang, X., Yu, S., and Zhang, X., The Gravitational-Wave Physics II: Progress, arXiv:2106.10235
- Boersma, O., Nichols, D. and Schmidt, P. 2020, Forecasts for detecting the gravitational-wave memory effect with Advanced LIGO and Virgo, *Phys. Rev. D* 101, 083026 (2020), arXiv:2002.01821
- Braginsky, V., Thorne, K. Gravitational-wave bursts with memory and experimental prospects. *Nature* 327, 123–125 (1987). <https://doi.org/10.1038/327123a0>
- Christodoulou, D., 1991, *Phys. Rev. Lett.* 67, 1486
- Claerbout, J. and Muir, F. 1973, Robust Modeling with Erratic Data, *Geophysics*, 38, 812-985
- Divakarla, A. and Whiting, B. 2021, The First-Order Velocity Memory Effect from Compact Binary Coalescing Sources, arXiv:2106.05163
- Ebersold, M. and Tiwari, S., 2020, Search for nonlinear memory from subsolar mass compact binary mergers, *Phys. Rev. D* 101, 104041
- Favata, M. 2009, *J. Phys. Conf. Ser.* 154, 012043
- Favata, M. 2010, *Class. quant. Grav.* 27:084036; see also <http://www.phy.olemiss.edu/StrongBaD/talks/Favata.pdf>
- Flanagan, E., Grant, A., Harte, A. and Nichols, D. 2019, Persistent gravitational wave observables: General framework *Phys. Rev. D*, 99, 084044
- Flanagan, E., Grant, A., Harte, A. and Nichols, D. 2020, Persistent gravitational wave observables: Nonlinear plane wave spacetimes *Phys. Rev. D*, 101, 104033
- Garfinkle, D. 2016, A simple estimate of gravitational wave memory in binary black hole systems, arXiv:1605.06687
- Grant, A. and Nichols, D. 2021, Persistent gravitational wave observables: Curve deviation in asymptotically flat spacetimes, arXiv: 2109.03832
- Gravitational Wave Open Science Center (GWOSC) <https://www.gw-openscience.org/eventapi/html/GWTC/> and https://losc.ligo.org/s/events/GW150914/GW150914_4_NR_
- Hübner, M., Talbot, C., Lasky, P. and Thrane, E. 2020, Measuring gravitational-wave memory in the first LIGO/Virgo gravitational-wave transient catalog *Phys. Rev. D* 101, 023011
- Hübner, M., Paul Lasky, and Eric Thrane, E. 2021, Memory remains undetected: Updates from the second LIGO/Virgo gravitational-wave transient catalog *Phys. Rev. D* 104, 023004
- Islo, K., Simon, J., Burke-Spolaor, S., and Siemens, X. 2019, Prospects for Memory Detection with Low-Frequency Gravitational Wave Detectors, arXiv:1906.11936
- Johnson, A., Kapadia, S., Osborne, A., Hixon, A., and Kennefick, D. 2019, Prospects of detecting the nonlinear gravitational wave memory," *Phys. Rev. D* 99, 044045 (2019), arXiv:1810.09563 [gr-qc].
- Kennefick, D. 1994, Prospects for detecting the Christodoulou memory of gravitational waves from a coalescing compact binary and using it to measure neutron star radii, *Phys. Rev. D* 50, 3587–3595 (1994).
- Khera, N., Krishnan, B., Ashtekar, A. and De Lorenzo, T. (2021) Inferring the gravitational wave memory for binary coalescence events *Physical Review D*, 103, 044012
- Kumar, S, 2021, Displacement memory and BMS symmetries, arXiv: 2109.13082
- Lasky, P., Thrane, E., Levin, Y., Blackman, J/, and Chen, Y. 2016, Detecting gravitational wave memory with LIGO: implications of GW150914, *Phys. Rev. Lett.* 117, 061102 (2016), arXiv:1605.01415
- Liu, X., He, X., and Cao Z., 2021, Accurate calculation of gravitational wave memory, *Phys. Rev. D* 103, 043005
- Lomb, N. R. 1976, *Ap&SS*, 39, 447

⁶ Amusingly this word is lightly embossed on the cover of some editions.

- McKechan, D., Robinson, C. and Sathyaprakash, B. 2010, A tapering window for time-domain templates and simulated signals in the detection of gravitational waves from coalescing compact binaries *Class.quant.*, 27:084020
- Mitman, K., Iozzo, D., Khera, N., Boyle, M., De Lorenzo, T., Deppe, N., Kidder, L., Moxon, J., Pfeiffer, H., Scheel, M., Teukolsky, S., and Throwe, W. 2021, Adding gravitational memory to waveform catalogs using BMS balance laws, *Physical Review D*, Volume 103, Issue 2, article id.024031
- Percival, D., and Walden, A. 1993, *Spectral Analysis for Physical Applications: Multitaper and Conventional Univariate Techniques*. Cambridge: Cambridge University Press, 1993.
- Pollney, D. and Reisswig, C.(2011), Gravitational Memory in Binary Black Hole Mergers, *ASp. J.*, 732, L13,
- Scargle, J. 1982, Studies in Astronomical Time Series Analysis: II. Statistical Aspects of Spectral Analysis of Unevenly Spaced Data, *ApJ*, 263, 835-853.
- Scargle, J. 1989, Studies in astronomical time series analysis. III. Fourier Transforms, Autocorrelation Functions, and Cross-Correlation Functions of Unevenly Spaced Data. *ApJ*, 343, 874-887
- Slepian, D, 1978, Prolate spheroidal wave functions, fourier analysis, and uncertainty — V: the discrete case,” *The Bell System Technical Journal*, 57, 1371-1430
- Talbot, C., Thrane, E., Lasky, P. and Lin, F. 2018, Gravitational-wave memory: waveforms and phenomenology *Phys. Rev. D* 98, 064031
- Spectrum estimation and harmonic analysis, Thomson, D. J. (1982) *Proceedings of the IEEE*, 70, 1055–1096
- Thorne, K. Gravitational-wave bursts with memory: The Christodoulou effect, 1987, *Physical Review D*, 45, 520
- Tiwari, S., Ebersold, M., and Hamilton, E. 2021, Leveraging gravitational-wave memory to distinguish neutron star–black hole binaries from black hole binaries, *arXiv: 2110.11171*
- Yang, H. and Martynov, D(2018) Testing Gravitational Memory Generation with Compact Binary Mergers, *Physical Review Letters*, 121, 071102
- Zhang, P., Duval, C., Gibons, G. and Horvathy, P., 2017, *Physics Letters B*, 772, 743
- Zhao, Z., Liu, X., Cao, Z. and He, X., 2021) Gravitational wave memory of the binary black hole events in GWTC-2, *Physical Review D.*, 104, 064056
- Zhao, Z., Cao, 2021) Stochastic gravitational wave background due to gravitational wave memory, *arXiv: 2111.13883*

5. APPENDIX A: STRAIN OFFSET MEASUREMENTS

Table 1. Strain Offset Measurements (10^{-22})

No.	ID	T_0	T_{start}	T_{stop}	Code	Weighted	Average	Linear	Fit	h(max)
						Δ h	σ	Δ h	σ	
1	150914	1126259462.0	0.330	0.430	HS1Ov	-0.328	0.2691	-0.610	0.5141	51.664
2			0.320	0.425	LS3P	-0.883	0.2593	-1.962	0.4970	41.838
3	151012	1128678900.0	0.410	0.437	HS1P	-0.199	0.3025	-0.306	0.5297	18.797
4			0.390	0.422	LS2NOv	0.321	0.3438	0.299	0.5919	19.945
5	151226	1135136350.0	0.360	0.640	LS2P	0.456	0.3594	0.793	0.6451	39.834
6	170104	1167559936.0	0.580	0.595	HS2Ov	0.051	0.3355	0.368	0.5734	24.651
7			0.570	0.600	LS1P	0.427	0.1974	0.750	0.3324	17.510
8	170608	1180922494.0	0.215	0.476	LTP	0.375	0.7799	0.805	1.3335	18.921
9	170729	1185389807.0	0.290	0.330	HS1Ov	0.639	0.3435	1.218	0.5975	22.705
10			0.280	0.314	LS1NOv	0.018	0.2152	-0.656	0.3717	13.262
11	170809	1186302520.0	-0.277	-0.258	HTP	0.364	1.0999	0.981	1.8700	32.569
12	170814	1186741861.0	0.450	0.535	HS1NOv	0.400	0.3163	0.353	0.5407	22.939
13			0.460	0.525	LS1P	0.142	0.2227	0.027	0.3821	24.580
14			0.580	0.605	VS1P	-0.504	0.6853	-0.649	1.1611	51.205
15	170818	1187058327.0	0.035	0.080	LS3P	-0.151	0.1773	-0.122	0.3000	24.190
16	170823	1187529256.0	0.500	0.515	HS1NOv	-0.843	0.3476	-1.093	0.5784	25.200
17			0.450	0.517	LS1Ov	0.135	0.2850	0.117	0.4760	23.361
18	190408	1238782700.0	0.100	0.275	HS1P	-0.432	0.2145	-1.153	0.3631	20.747
19			0.115	0.288	LS1Ov	0.190	0.2232	0.319	0.3806	22.009
20	190412	1239082262.0	0.000	0.165	LS1NOv	-0.232	0.3984	-0.410	0.6810	16.683
21	190413	1239198206.0	0.720	0.740	HS1NOv	-0.195	0.3140	-0.319	0.5343	12.036
22			0.710	0.738	LS1NOv	-0.007	0.1754	0.149	0.2967	17.718
23	190421	1239917954.0	0.195	0.255	LS1NOv	0.018	0.1582	-0.077	0.2682	9.363
24	190424	1240164426.0	0.060	0.147	LS2Ov	0.015	0.1813	-0.153	0.3087	15.429
25	190503	1240944862.0	0.255	0.300	HS2NOv	0.004	0.2209	-0.145	0.3774	17.845
26			0.270	0.290	LTNOv	-0.116	1.1535	-0.702	1.9716	19.912
27	190512	1241719652.0	0.260	0.420	HS1P	0.074	0.2614	0.036	0.4543	16.509
28			0.250	0.420	LS1Ov	-0.090	0.2045	-0.351	0.3567	10.690
29	190514	1241852074.0	0.795	0.845	HS2Ov	-0.293	0.2143	-0.752	0.5629	13.556
30	190517	1242107480.0	-0.200	-0.180	LS2P	-0.124	0.1483	-0.434	0.3804	20.534
31	190519	1242315362.0	0.355	0.393	HS1NOv	0.463	0.2556	0.833	0.6478	22.630
32	190521	1242459857.0	0.435	0.465	HS1NOv	-0.305	0.1919	-0.551	0.4778	25.153
33			0.345	0.465	LS1Ov	-0.007	0.1938	-0.110	0.4801	28.111
34	190522a	1242442967.0	0.420	0.455	HS2P	-0.348	0.1674	-0.593	0.4094	17.567
35			0.405	0.470	LS1Ov	0.342	0.1747	0.790	0.4246	15.672
36	190527	1242984074.0	-0.264	-0.235	HS1P	-0.296	0.8109	-0.631	1.9648	15.419
37			-0.235	-0.217	LS1Ov	-0.070	0.1439	0.188	0.3434	10.796
38	190602	1243533585.0	0.050	0.110	HS2Ov	0.067	0.1847	-0.022	0.4382	11.320
39			0.050	0.100	LS3P	-0.193	0.2980	-0.154	0.7039	14.651
40	190620	1245035079.0	0.240	0.315	LS1Ov	-0.215	0.1960	-0.651	0.4588	17.714
41	190630	1245955943.0	0.050	0.180	LS1NOv	-0.073	0.2384	-0.114	0.5564	27.844
42	190701	1246048404.0	0.510	0.570	HS1NOv	0.244	0.1690	0.277	0.3924	12.230
43			0.540	0.590	VS3P	0.550	0.3300	0.837	0.7610	27.853
44	190706	1246487219.0	0.290	0.330	HS1NOv	-0.598	0.1716	-0.757	0.3931	14.410

No.	ID	T_0	T_{start}	T_{stop}	Code	Δ h	σ	Δ h	σ	
45			0.280	0.330	LS1NOv	0.355	0.1998	0.358	0.4539	14.737
46	190707	1246527224.0	0.030	0.165	HS1NOv	0.227	0.2746	0.183	0.6226	12.415
47			-0.030	0.170	LS1Ov	-0.185	0.2452	-0.405	0.5552	12.192
48	190708	1246663515.0	0.225	0.385	LS1Ov	-0.086	0.2668	0.038	0.6086	15.473
49	190727	1248242632.0	-0.060	-0.010	HS2NOv	-0.009	0.2707	-0.194	0.6088	22.406
50			-0.050	-0.010	LS2P	-0.250	0.1364	-0.130	0.3045	12.993
51	190728	1248331528.0	0.390	0.520	HS1NOv	-0.099	0.2098	0.086	0.4672	11.332
52			0.240	0.525	LS1NOv	0.020	0.1472	-0.136	0.3274	11.044
53	190803	1248834440.0	-0.150	-0.110	HS1NOv	0.192	0.2802	0.519	0.7244	14.080
54	190814	1249852257.0	-0.300	0.010	HTOv	0.051	0.3948	-0.017	1.0189	16.341
55			-0.300	0.020	VTP	-0.657	2.2315	-0.899	5.7500	59.872
56	190828	1251009264.0	-0.390	-0.240	HS2P	-0.169	0.1444	-0.194	0.3705	17.472
57			-0.380	-0.240	LS1Ov	-0.240	0.1713	-0.382	0.4385	16.445
58	190909	1252064527.0	0.685	0.715	HS1NOv	0.026	0.2580	-0.102	0.6592	15.676
59			0.685	0.710	LS1Ov	-0.183	0.2564	-0.112	0.6515	10.737
60	190910	1252150105.0	0.240	0.334	LS1Ov	0.038	0.1670	0.434	0.4228	19.125
61	190915	1252627040.0	0.650	0.695	HS2NOv	-0.260	0.2318	-0.981	0.5866	21.688
62			0.600	0.700	LS1Ov	0.428	0.1847	0.683	0.4662	11.427
63	190929	1253755327.0	0.425	0.520	HS1Ov	-0.095	0.1857	-0.025	0.4670	10.929
64			0.390	0.500	LS1NOv	-0.174	0.1972	-0.275	0.4945	13.216
65	191223	1261100537.0	0.555	0.635	LS3P	-0.098	0.4101	-0.203	1.0214	29.146
66	191225	1261346254.0	-0.200	-0.130	VS3P	-1.224	0.2911	-2.327	0.7221	33.170
67	200114	1263002916.0	0.090	0.370	LS2P	-0.225	0.1747	-0.457	0.4325	29.992

Note: For two strain offset metrics (weighted mean, linear fit) the strain offset and its 1σ standard error are given, both scaled to 10^{-22} . In the code, OTW, O is the observatory (Hanford, Livingston, Virgo), and the optimized values are: T denotes the optimal taper: T = Tukey, Sn = Slepian of order n; W indicates the whitening method: Ov = Welch-like, 2-second overlap, NO = Welch-like with no overlap, P = unsmoothed spectrum (“phase only”). After an index are the GWOSC event ID and the fiducial event GPS time T_0 in seconds (this is not the time at which the 4096 observation begins), both from the GWOSC web site, and the start and stop times relative to T_0 adopted here for the merger chirp signal.

6. APPENDIX B: FOURIER TRANSFORM OF ARBITRARILY SPACED DATA (MATLAB CODE)

```
function ft_vec = ft_uneven( data_in )
```

```
%-----
%           Complex Fourier Transform of arbitrarily spaced data
%.       (Translated and Updated from ApJ 343, 1989, 874-887, Paper III)
%-----
% Input: data_in.xx_vec  -- Dependent variable samples
%        data_in.tt_vec  -- Corresponding sample times
%        data_in.ww_vec  -- Evaluate at these frequencies (radians per unit time)
%        data_in.ft_sign -- Sign of the transform
%        data_in.tt_zero -- Origin of time
%-----
% Output:          ft_vec -- Fourier transform (complex)
%-----

xx_vec = data_in.xx_vec; tt_vec = data_in.tt_vec; ww_vec = data_in.ww_vec;
ft_sign = data_in.ft_sign; tt_zero = data_in.tt_zero;
num_xt = length( xx_vec );    % number of samples
num_ww = length( ww_vec );    % number of frequencies
ft_vec = zeros( num_ww, 1 );

for ii_ww = 1: num_ww          % Start Frequency Loop

    wrun = ww_vec( ii_ww );

    if wrun == 0
        ft_vec( ii_ww ) = sum( xx_vec ) / sqrt( num_xt );
        ls_vec( ii_ww ) = ft_vec( ii_ww ) .^2;
    else
        csum = sum( cos( 2.0 * wrun * tt_vec ) );
        ssum = sum( sin( 2.0 * wrun * tt_vec ) );
        wtau = 0.5 * atan2( ssum, csum );
        sumr = sum( xx_vec .* cos( wrun * tt_vec - wtau ) );
        sumi = sum( xx_vec .* sin( wrun * tt_vec - wtau ) );
        scos2 = sum( ( cos( wrun * tt_vec - wtau ) ) .^ 2 );
        ssin2 = sum( ( sin( wrun * tt_vec - wtau ) ) .^ 2 );
        ft_real = sumr / ( sqrt(2) * sqrt( scos2 ) );
        ft_imag = ft_sign * sumi / ( sqrt(2) * sqrt( ssin2 ) );
        phase_this = wtau - wrun * tt_zero;
        ft_vec( ii_ww ) = complex( ft_real, ft_imag ) * exp( 1i * phase_this );
    end
end

end
```

7. APPENDIX C: SHIFT MERGER EVENT TO THE CENTER OF THE DATA ARRAY

These code fragments shift the event center to the center of the observation. Functions `shift_with_extrap` and `ar_extrap` implement a straightforward autoregressive extrapolation at the vacated end.

```
% Shift the event to the center of the strain time series
% id_11 and id_22 are the indices marking the start and stop of merger
sample_rate = 16384;      % 16 kHz samples
num_total    = 67108864;% length of time series
shift_by = fix( ( num_total/2 ) - 0.5*( id_11 + id_22 ) );

% Choice 1: Shift and cut
num_ends = 2 * sample_rate; % Cut off 2 seconds at both ends
iu = num_ends + 1: num_total - num_ends;
strain = strain( iu - shift_by );
id_11 = id_11 + shift_by - num_ends;% Adjust merger indices for the shift
id_22 = id_22 + shift_by - num_ends;

% Choice 2: Shift and extrapolate
strain = shift_with_extrap( strain, rotate_by );
id_11 = id_11 + shift_by;id_22 = id_22 + shift_by;
-----
function strain = shift_with_extrap( strain, shift_by )
if shift_by < 0
    strain = ar_extrap( strain, -shift_by );
    strain = strain( -shift_by+1: end );
else
    strain = strain( end: -1: 1);
    strain = ar_extrap( strain, shift_by );
    strain = strain( shift_by + 1: end );
    strain = strain(end: -1: 1);
end

function strain = ar_extrap( strain, num_ext)
fit_ord = 8;% default order
aa = aryule( strain, fit_ord );% Matlab's Yule-Walker solution for AR(8)
aa = aa(end:-1:2);% select the prediction segment of the AR array
mm_ex = length( aa ) - 1;
strain_len = length( strain );
strain = [ strain NaN* ones( 1, num_ext ) ];
for ii_ext = 1: num_ext % Predictive convolution
    id_end = strain_len + ii_ext - 1;
    id_start = id_end - mm_ex;
    strain_this = strain( id_start: id_end );
    strain( strain_len + ii_ext ) = -sum( aa(:) .* strain_this(:) );
end
```

8. APPENDIX D: SHIFT ENDPOINTS TO OSCILLATION NODES

This function shifts the initial choices for the end points of the averaging intervals to the nearest node of the whitened and filtered time series. The goal is to minimize any contribution of the merger “chirp signal” to the estimated memory offset. The start and end points of the pre-event (post-event) averaging intervals are shifted to the nearest previous (subsequent) zero crossing. All four points are thus moved slightly further from the event itself.

```
function [ jj_00, jj_11, jj_22, jj_33 ] = find_nodes( strain_vec, num_use, ii_00, ii_11, ii_22, ii_33 )
% Shift start/end points to nearest nodes away from the event
% Inputs: strain_vec    full strain time series
%         num_use       length of small working interval
%         ii_00         start of pre-event interval
%         ii_11         end of pre-event interval
%         ii_22         start of post-event interval
%         ii_33         end of post-event interval
%
% Output: input intermarkers shifted to nodes
%-----

% Cut out local working interval:

id_begin = ii_00 - num_use;
id_end   = ii_33 + num_use;

strain_vec = strain_vec( id_begin: id_end );
num_total = length( strain_vec );

% adjust strain array to have zero mean over a sub-interval
mean_adjust = mean( strain_vec );
strain_vec = strain_vec - mean_adjust;

% id_begin is also offset for all indices

ii_00 = ii_00 - id_begin;
ii_11 = ii_11 - id_begin;
ii_22 = ii_22 - id_begin;
ii_33 = ii_33 - id_begin;

% start of pre-event
if strain_vec( ii_00 ) < 0
    strain_vec = - strain_vec;% Make strain at this point positive
end
% Previous sign change
jj_00 = find( (1:num_total) < ii_00 & strain_vec(:)' < 0 );
jj_00 = jj_00(end);
```

```

% end of pre-event
if strain_vec( ii_11 ) < 0
    strain_vec = - strain_vec;% Make strain at this point positive
end
% Previous sign change
jj_11 = find( (1:num_total) < ii_11 & strain_vec(:)' < 0 );
jj_11 = jj_11(end);

%-----

% Start of post-event
if strain_vec( ii_22 ) < 0
    strain_vec = - strain_vec;% Make strain at this point positive
end
% Subsequent sign change
jj_22 = find( (1:num_total) > ii_22 & strain_vec(:)' < 0 );
jj_22 = jj_22(1)-1;

% End of post-event
if strain_vec( ii_33 ) < 0
    strain_vec = - strain_vec;% Make strain at this point positive
end
% Subsequent sign change
jj_33 = find( (1:num_total) > ii_33 & strain_vec(:)' < 0 );
jj_33 = jj_33(1)-1;

jj_00 = jj_00 + id_begin;% Restore offsets
jj_11 = jj_11 + id_begin;
jj_22 = jj_22 + id_begin;
jj_33 = jj_33 + id_begin;

```

9. APPENDIX E: WHITENING WITH TAPERS

The slepian tapers are pre-computed using the Matlab function `dpss`, in the form `dpss_use = dpss(num_total, nw, 3)`. yielding the first three orders, with bandwidth `nw`.

```

data_welch_in.xx = strain_raw;
data_welch_in.dt_shift = 2 * sample_rate;    % 2 second shift
data_welch_in.block_length = 4 * sample_rate;% 4 second block

for ii_taper = 1: num_tapers_total

    if ii_taper <= num_tapers

        % Welch/thompson with overlap
        data_welch_in.id_taper = ii_taper;
        data_welch_in.dt_shift = 2 * sample_rate;    % 2 second shift
        data_welch_in.block_length = 4 * sample_rate;% 4 second blocks
        data_welch_out = my_multitaper_welch( data_welch_in );
        sp_welch = data_welch_out.sp_vec;
        sp_use = interp1( id_in, sp_welch, id_out, 'pchip' )';

        strain_white = real( ifft( ...
            fft( strain_raw .* tukeywin( num_total ) ) ./ sp_use ) );

    elseif ii_taper <= 2 * num_tapers

        % welch/thompson with no overlap
        data_welch_in.id_taper = ii_taper - num_tapers;
        data_welch_in.dt_shift = 0;    % 2 second shift
        data_welch_in.block_length = 0;% 4 second blocks
        data_welch_out = my_multitaper_welch( data_welch_in );
        sp_welch = data_welch_out.sp_vec;
        sp_use = interp1( id_in, sp_welch, id_out, 'pchip' )';

        strain_white = real( ifft( ...
            fft( strain_raw .* tukeywin( num_total ) ) ./ sp_use ) );

    else

        % "Phase only" whitening
        if ii_taper == 2*num_tapers + 1
            % Tukey
            strain_white = ...
                real( ifft( exp( 1i * angle( fft( strain_raw .* tukey_window ) ) ) ) );
        elseif ii_taper == 2*num_tapers + 2
            % one Slepian
            strain_white = ...
                real( ifft( exp( 1i * angle( fft( strain_raw .* dpss_use(:,1) ) ) ) ) );
        elseif ii_taper == 2*num_tapers + 3

```

```

% 2 Slepians
strain_white = strain_white + ...
real( ifft( exp( 1i * angle( fft( strain_raw .* dpss_use(:,2) ) ) ) ) );
strain_white = strain_white + ...
    real( ifft( exp( 1i * angle( fft( strain_raw .* ...
        dpss_use(end:-1:1,2) ) ) ) ) );
elseif ii_taper == 2*num_tapers + 4
    % 3 Slepians
    strain_white = strain_white + ...
    real( ifft( exp( 1i * angle( fft( strain_raw .* dpss_use(:,3) ) ) ) ) );
    end
end
end

```

10. APPENDIX F: BLOCK AVERAGING OF AMPLITUDE SPECTRA A LA WELCH

This function implements simple block averages, with or without overlap of the blocks.

```
function data_out = my_multitaper_welch( data_in )

global dpss_block nw tukey_block_window % these are in common memory

xx = data_in.xx;% time series
mm = data_in.mm;% number of blocks
id_taper = data_in.id_taper;b% choice of taper

if isfield( data_in, 'dt_shift' );
    dt_shift = data_in.dt_shift;
    block_length = data_in.block_length;
else
    dt_shift = 0;
end
%=====
%
% Define tapers from value of id_taper
% 0 = none;
% 1 = Tukey
% 2 = 1 Discrete prolate spheroidal (Slepian) sequence
% 3 = 2 Discrete prolate spheroidal (Slepian) sequences
% 4 = 3 Discrete prolate spheroidal (Slepian) sequences
%
%=====
if dt_shift == 0

    num_total = length( xx );
    block_length = fix( num_total / mm );

    if id_taper >= 2
        % Compute Slepian
        if isempty( dpss_block ) | length( dpss_block ) ~= block_length
            disp('doing slepian')
            nw = 2.5;
            dpss_block = dpss( block_length, nw, 3 );
        end
    end

    if isempty( tukey_block_window ) | length( tukey_block_window ) ~= block_length
        disp('tukey window')
        tukey_block_window = tukeywin( block_length, 1 );
    end
end
```

```

id_start_vec = 1: block_length: num_total;
id_stop_vec  = id_start_vec + block_length - 1;
sp_vec = zeros( block_length, 1 );

for ii_spec = 1: mm

    id_start = id_start_vec( ii_spec );
    id_stop  = id_stop_vec(  ii_spec );
    xx_block = xx( id_start: id_stop );

    if id_taper == 0    % no taper
        sp_vec = sp_vec + abs( fft( xx_block ) );
    end

    if id_taper == 1
        % Tukey(1)
        sp_vec = sp_vec + abs( fft( xx_block .* tukey_block_window ) );
    end

    if id_taper == 2    % 1 Slepian
        sp_vec = sp_vec + abs( fft( xx_block .* dpss_block(:,1) ) );
    end

    if id_taper == 3    % 2 Slepians
        sp_this =          abs( fft( xx_block .* dpss_block(    :,      1) ) );
        sp_this = sp_this + abs( fft( xx_block .* dpss_block(    :,      2) ) );
        sp_this = sp_this + abs( fft( xx_block .* dpss_block(end:-1:1, 2) ) );
        sp_this = sp_this / 3;
        sp_vec = sp_vec + sp_this;
    end

    if id_taper == 4    % 3 Slepians
        sp_this =          abs( fft( xx_block .* dpss_block(    :,      1) ) );
        sp_this = sp_this + abs( fft( xx_block .* dpss_block(    :,      2) ) );
        sp_this = sp_this + abs( fft( xx_block .* dpss_block(end:-1:1, 2) ) );
        sp_this = sp_this + abs( fft( xx_block .* dpss_block(    :,      3) ) );
        sp_this = sp_this / 4;
        sp_vec = sp_vec + sp_this;
    end
end
data_out.sp_vec = sp_vec / mm;
return
else % overlap

%=====
% for overlap
% T = total interval

```

```

% dt_window = 4 sec
% dt_shift  = 2 sec
% id_start = 1 + dt_shift * ( ii - 1 )
% id_stop  = 1 + dt_shift * ( ii - 1 ) + dt_window - 1;
%=====

    num_total = length( xx );
    id_start_vec = 1: dt_shift: 2*num_total;% extra!
    id_stop_vec  = id_start_vec + block_length - 1;
    iu = find( id_stop_vec <= num_total );
    id_start_vec = id_start_vec(iu);
    id_stop_vec  = id_stop_vec(iu);
    mm = length( id_start_vec );

    if id_taper >= 2
        % Compute Slepians
        if isempty( dpss_block ) | length( dpss_block ) ~= block_length
            disp('doing slepians')
            nw = 2.5;
            dpss_block = dpss( block_length, nw, 3 );
        end
    end

    if isempty( tukey_block_window ) | length( tukey_block_window ) ~= block_length
        disp('tukey window')
        tukey_block_window = tukeywin( block_length, 1 );
    end

    sp_vec = zeros( block_length, 1 );

    for ii_spec = 1: mm

        id_start = id_start_vec( ii_spec );
        id_stop  = id_stop_vec(  ii_spec );
        xx_block = xx( id_start: id_stop );

        if id_taper == 0      % no taper
            sp_vec = sp_vec + abs( fft( xx_block ) );
        end

        if id_taper == 1
            % Tukey(1)
            sp_vec = sp_vec + abs( fft( xx_block .* tukey_block_window ) );
        end

        if id_taper == 2      % 1 Slepian
            sp_vec = sp_vec + abs( fft( xx_block .* dpss_block(:,1) ) );
        end
    end

```

```

end

if id_taper == 3    % 2 Slepians
    sp_this =          abs( fft( xx_block .* dpss_block(    :,    1) ));
    sp_this = sp_this + abs( fft( xx_block .* dpss_block(    :,    2) ));
    sp_this = sp_this + abs( fft( xx_block .* dpss_block(end:-1:1, 2) ));
    sp_this = sp_this / 3;
    sp_vec = sp_vec + sp_this;
end

    if id_taper == 4    % 3 Slepians
        sp_this =          abs( fft( xx_block .* dpss_block(    :,    1) ));
        sp_this = sp_this + abs( fft( xx_block .* dpss_block(    :,    2) ));
        sp_this = sp_this + abs( fft( xx_block .* dpss_block(end:-1:1, 2) ));
        sp_this = sp_this + abs( fft( xx_block .* dpss_block(    :,    3) ));
        sp_this = sp_this / 4;
        sp_vec = sp_vec + sp_this;
    end
end

data_out.sp_vec = sp_vec / mm;

```